NUCL SCI TECH (2018) 29:11
https://doi.org/10.1007/s41365-017-0342-4

Characterization of the new scintillator $Cs_2LiYCl_6:Ce^{3+}$

Kui-Nian Li[1] · Xian-Peng Zhang[1,2] · Qiang Gui[3] · Peng Jin[1] · Geng Tian[1]

Received: 6 November 2016 / Revised: 1 April 2017 / Accepted: 6 April 2017 / Published online: 29 December 2017

Abstract The first domestic inorganic scintillator, $Cs_2LiYCl_6:Ce^{3+}$ (CLYC), was grown at Beijing Glass Research Institute using the vertical Bridgman method. In this work, we evaluated the performance of this new CLYC crystal in terms of its gamma-ray energy resolution and pulse shape discrimination (PSD) capability between neutrons and gamma rays. The decay times associated with different scintillation mechanisms were obtained by fitting decay functions to the neutron and gamma-ray waveform structures. We found an energy resolution of $\sim$ 4.5% for 662-keV gamma rays and efficient neutron/gamma PSD with a figure of merit of $\sim$ 2.6. Under gamma-ray excitation, there is an ultrafast scintillation mechanism in CLYC with a decay time of approximately 2 ns, whereas there is no evidence of ultrafast decay under thermal neutron excitation. This work contributes to the promotion of domestic development of CLYC.

Keywords $Cs_2LiYCl_6:Ce^{3+}$ · Energy resolution · Pulse shape discrimination · Decay time · Thermal neutrons

1 Introduction

$Cs_2LiYCl_6:Ce^{3+}$ (CLYC) [1] is a promising new inorganic scintillator. It was first discovered as a scintillator in 1999 by researchers from Delft University of Technology [2]. They reported that CLYC was capable of thermal neutron detection based on the $^6Li(n,\alpha)t$ reaction and made further investigations of CLYC in the next few years [3–5]. Van Loef et al. [6] revealed the scintillation mechanism of CLYC, known as core-to-valence luminescence (CVL), in 2005. CVL has an ultrafast decay time ($\sim$ ns) and appears only under gamma-ray irradiation [7]. Thus, CVL makes it possible to use CLYC to discriminate between neutron (alpha and triton) particles and gamma rays by pulse shape discrimination (PSD) methods [8]. The PSD capability of CLYC attracted strong attention from the nuclear science community [9–14]. Under gamma-ray irradiation, its light yield is about 20,000 photons/MeV [15], and it exhibits a good energy resolution of $\sim$ 4%, which is the full-width at half-maximum (FWHM) at 662 keV owing to proportional linearity [16]. Under thermal neutron irradiation, the light yield is about 70,500 photons per neutron. The thermal neutron peak resolution is typically 2.5–3.1% [9] at approximately 3.4 MeV (gamma equivalent energy).

Radiation Monitoring Devices Inc. grew its first CLYC crystal in 2003. Since then, a number of CLYC crystals with different sizes and features have been grown as crystal growth technology has developed [17–20]. In 2012, CLYC became commercially available, but the price was still high. To establish domestic CLYC growth technology, Beijing Glass Research Institute (BGRI) grew a promising CLYC crystal in 2016. To our knowledge, it is the first domestically developed CLYC crystal. To evaluate the performance of the new CLYC crystal, we focused on two

This work was supported by the National Natural Science Foundation of China (No. 11575145).

✉ Kui-Nian Li
lk.nian@foxmail.com

[1] Northwest Institute of Nuclear Technology, Xi'an 710024, China

[2] School of Nuclear Science and Technology, Xi'an Jiaotong University, Xi'an 710049, China

[3] Beijing Glass Research Institute, Beijing 101111, China

important properties: its gamma-ray energy resolution and PSD capability. Moreover, we obtained the decay times of different scintillation mechanisms by fitting exponential decay functions to the neutron and gamma-ray waveform structures.

2 Experimental

2.1 Crystal growth

The CLYC crystal was grown using the vertical Bridgman method at BGRI. In this method, stoichiometric amounts of CsCl, LiCl, YCl_3, and $CeCl_3$ (with a purity of 99.99%) were mixed in a quartz crucible. Natural LiCl with a ^{6}Li isotope content of approximately 7% was used. The dopant (Ce^{3+}) concentration was 0.5 mol% as a standard doping level. After the powders were mixed in the quartz crucible, the pressure was pumped to a vacuum of 10^{-5} Pa to avoid oxidization. The quartz crucible was sealed, and the mixed powders were fused in a stove at a temperature above 640 °C. As the quartz crucible was steadily lowered at a velocity of 2 mm/h, a CLYC crystal ingot was grown.

After cutting and polishing, the CLYC crystal was packed in an aluminum casing with a reflective inner coating and sealed with a quartz window at one end. The packed crystal has a diameter of 25.4 mm and a thickness of 15 mm, as shown in Fig. 1. The density of the CLYC is 3.31 g/cm^3. The radioluminescence spectrum was measured by a Zolix Omni-λ300 monochromator under Cs gamma-ray irradiation, as shown in Fig. 2. The radioluminescence has two main components, one in the 290 nm range due to CVL and one in the 360–440 nm range due to Ce^{3+} ions, in good agreement with the spectra of many commercially available bialkali photomultiplier tubes

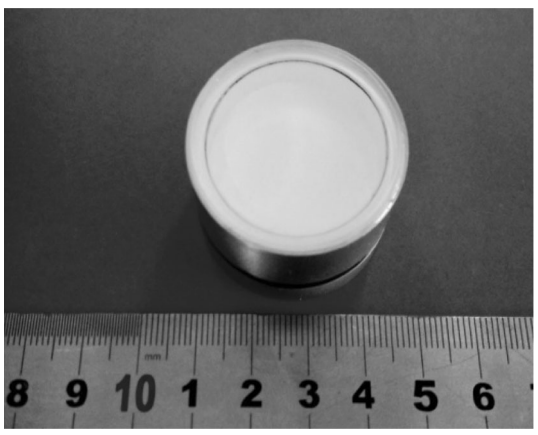

Fig. 1 Photograph of CLYC crystal 25.4 mm in diameter and 15 mm in thickness grown at BGRI. The crystal is packaged in an aluminum enclosure

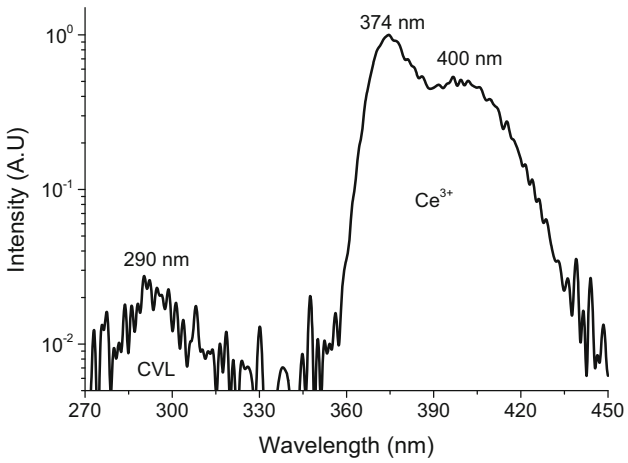

Fig. 2 Radioluminescence spectrum of CLYC crystal. The two main emission components are due to CVL and Ce^{3+} ions, respectively

(PMTs). In the range of 360–440 nm, two peaks at 374 and 400 nm were found, which are due to re-emission after self-absorption.

2.2 Data acquisition

The CLYC crystal was coupled with a 2-in.-diameter 9815B blue–green-sensitive bialkali PMT (Electron Tubes Inc.) with optical grease. The 9815B PMT's quantum efficiency is ∼ 30% at the peak emission wavelength of CLYC. To estimate the gamma-ray energy resolution of the CLYC crystal, a ^{137}Cs source was used. The signals from PMT anodes with different heights were analyzed by a multichannel analyzer. A shaping time of 4 μs was used on the spectroscopy amplifier.

An Am–Be source that emits approximately 1×10^4 neutrons per second was used as a neutron and gamma-ray source to estimate the PSD capability of CLYC. A schematic diagram of the experimental setup is shown in Fig. 3. A Tektronix DPO7104 oscilloscope was set to FastFrame mode (1 G samples per second and 2 μs recording length) to record the PMT anode signals from both neutrons and gamma rays with a 50-Ω terminator. The CLYC crystal coupled with the 9815B PMT was placed in a polyethylene tube. A polyethylene block 2.5 cm in thickness and a lead block 2.5 cm in thickness were placed between the CLYC crystal and the Am–Be source. Approximately 5000 signals were recorded and then analyzed offline as described in Sect. 3.2.

3 Results and analysis

3.1 Gamma-ray energy resolution

Figure 4 shows the energy spectrum measured with the CLYC crystal under irradiation from the ^{137}Cs gamma-ray

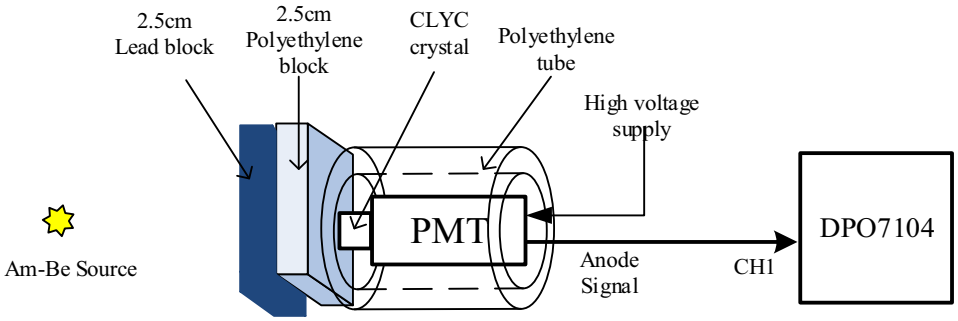

Fig. 3 (Color online) Experimental setup with Am–Be source. The CLYC crystal was coupled with a 9815B PMT, which was connected directly to a digital oscilloscope (Tektronix DPO7104)

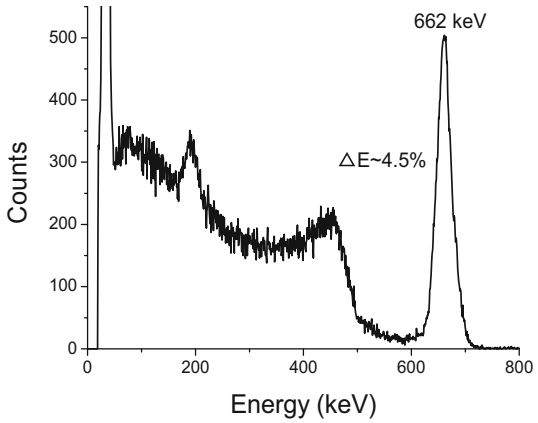

Fig. 4 ^{137}Cs energy spectrum measured with CLYC crystal. An energy resolution of ~ 4.5% (FWHM) at 662 keV was obtained

(662 keV) source. The position of the 662 keV energy peak was used to scale the horizontal axis in energy units (keV). The CLYC energy resolution at the 662 keV full energy peak is ~ 4.5% (FWHM), which is better than those of scintillators commonly used for gamma detection, such as NaI(Tl) and CsI(Tl), which have energy resolutions of 6.5 and 6% at 662 keV, respectively.

3.2 Neutron and gamma-ray discrimination

PSD was applied to separate gamma-ray waveforms from neutron waveforms using the traditional charge integration method. In this method, two integration windows of the signal pulses, the prompt integration window and delayed integration window, are selected and integrated. The prompt window includes the sharp rise and peak portion, and the delayed window includes the decaying portion of the signals. There are generally infinite combinations of possible integration window widths. It is essential to achieve the best possible PSD by optimizing the window widths. An automated waveform analysis algorithm can optimize the window width through the following procedure:

1. Align the waveforms to a common zero. The point where the amplitude was 20% of the peak value was chosen as the common zero.
2. Perform charge integration according to the two integration windows. The width of the prompt integration window ranged from 5 to 300 ns in 5 ns steps. The delayed integration window started immediately after the end point of the prompt window, and its width ranged from 10 to 1300 ns in 10 ns steps.
3. Calculate the PSD ratio. For each unique combination of the prompt and delayed integration windows, the PSD ratio was calculated for each waveform using the charge integrals Q_{prompt} and Q_{delayed}. The PSD ratio was defined as $Q_{\text{delayed}}/Q_{\text{prompt}}$.
4. Calculate the figure of merit (FoM). The FoM was utilized to evaluate the neutron and gamma-ray discrimination performance. It was defined as

$$\text{FoM} = \frac{D}{n_{\text{FWHM}} + \gamma_{\text{FWHM}}}, \quad (1)$$

where D is the distance between the centroids of the neutron and gamma peaks in the PSD ratio histogram, and n_{FWHM} and γ_{FWHM} are the corresponding FWHMs. To obtain the centroid positions and FWHMs, Gaussian fits were applied to the neutron and gamma-ray peaks in the histogram.

The result of the PSD optimization is shown in Fig. 5. This figure shows that the FoM is more sensitive to the prompt window width than to the delayed window width. With increasing prompt window width, the FoM shows a short, rapid increase, followed by a long, slow decrease. Changing the delayed window width has a minimal effect on the FoM. For the CLYC crystal in this study, the best FoM we found was 2.6, at a prompt window width of 20 ns and delayed window width of 900 ns.

Using the optimal prompt and delayed integration windows, a two-dimensional PSD scatter plot was generated for the neutron and gamma-ray events from an Am–Be source (Fig. 6). In Fig. 6, gamma-ray events and neutron events exhibit two distinct distribution patterns. Gamma-ray events have a lower PSD ratio across a wide energy

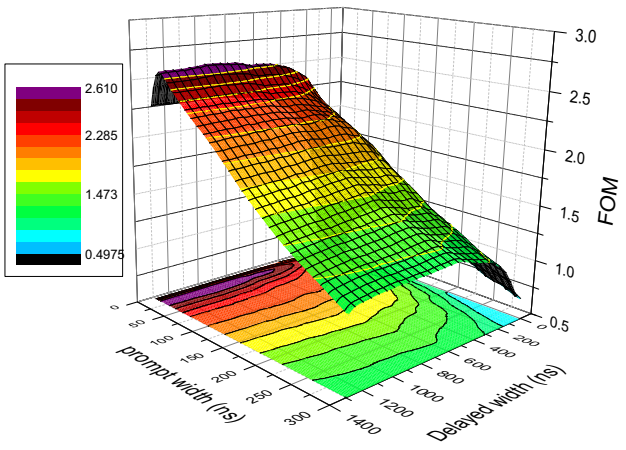

Fig. 5 (Color online) FoM under different prompt and delayed integration window combinations. The prompt window width ranges from 5 to 300 ns in 5 ns steps. The delayed window width ranges from 10 to 1300 ns in 10 ns steps

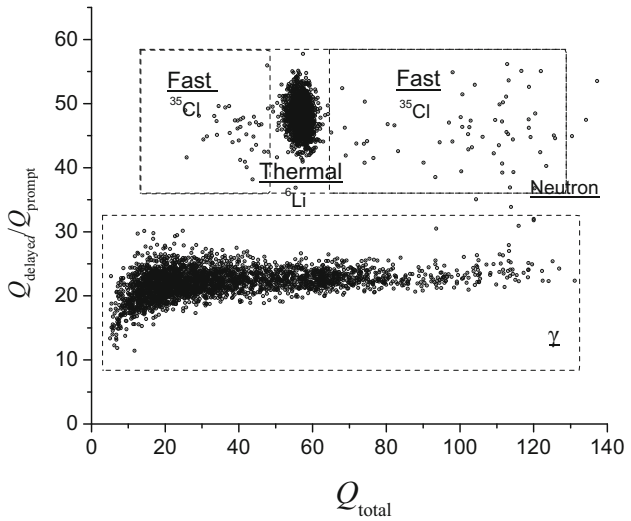

Fig. 6 Two-dimensional PSD scatter plot based on the data collected under irradiation from an Am–Be source. The *X* axis is the PSD ratio ($Q_{\text{delayed}}/Q_{\text{prompt}}$), and the *Y* axis is the total integral Q_{total} corresponding to the energy of the events. Gamma-ray events (bottom) and neutron events (top) are clearly separated. Fast neutrons (^{35}Cl) and thermal neutrons (^{6}Li) are indicated

range, whereas neutron events are isolated and have a higher PSD ratio. The neutron events can be divided into two groups representing different reactions [14]: fast neutrons and thermal neutrons, as indicated in Fig. 6. The thermal neutrons are produced by the ^{6}Li(n,α)t reaction, and the fast neutrons are from either the ^{35}Cl(n,p)^{35}S reaction or the ^{35}Cl(n,α)^{32}P reaction. Figure 7 (dashed line) shows the one-dimensional projection of the neutron and gamma-ray events to the *Y* axis in Fig. 6. A Gaussian function was fitted to the neutron and gamma-ray peaks in

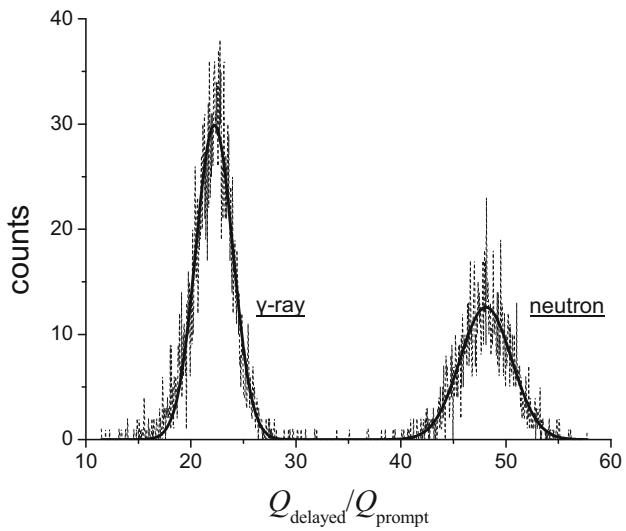

Fig. 7 One-dimensional projection of neutron and gamma-ray events to the *Y* axis in Fig. 6. A Gaussian function was fitted to the neutron and gamma-ray peaks (solid line)

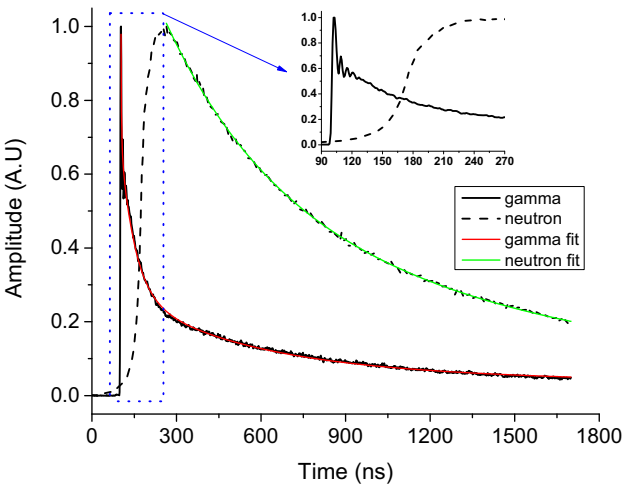

Fig. 8 (Color online) Overlay of neutron and gamma-ray standard pulses. The red and green lines are the gamma-ray and neutron standard pulse exponential fitting curves, respectively. Inset shows magnified view of the pulses at 90–270 ns

Fig. 7 (solid line). The centroids and FWHMs obtained from the Gaussian fits were used to calculate the FoM.

3.3 Pulse shape analyses

According to the optimal PSD results, neutron signals and gamma-ray signals were averaged separately to produce the standard pulses. The averaging process reduces the noise observed in the individual signals, making it easier to analyze them. The standard pulses, normalized by the maximum, are shown in Fig. 8. The characteristics of the neutron pulse and gamma-ray pulse exhibit significant

differences owing to their different scintillation mechanisms.

For a Ce^{3+}-doped CLYC crystal, up to four mechanisms generally contribute to the scintillation: Ce^{3+} (direct electron–hole capture by Ce^{3+}), V_k (binary V_k–electron diffusion), self-trapped exciton (STE) emission, and CVL. Detailed descriptions of those mechanisms can be found in Refs. [3, 10, 16].

To verify the scintillation mechanisms under neutron and gamma-ray excitation described in the literature, we used the exponential decay curves to fit the standard pulses (Fig. 8). Equation (2) was used to fit the gamma-ray standard pulse. There are four exponential decay components and thus four decay time constants. The decay time constant of each exponential component represents the decay time of the corresponding scintillation mechanism.

$$I_{\text{gamma}} = A_{g1}e^{-t/\tau_{g1}} + A_{g2}e^{-t/\tau_{g2}} + A_{g3}e^{-t/\tau_{g3}} + A_{g4}e^{-t/\tau_{g4}}, \quad (2)$$

where I_{gamma} is the amplitude of the gamma-ray standard pulse from the maximum point to the end; τ_{g1}, τ_{g2}, τ_{g3}, and τ_{g4} are the scintillation decay times for the CVL, Ce^{3+}, V_k, and STE mechanisms, respectively; and A_{g1}, A_{g2}, A_{g3}, and A_{g4} are the amplitudes of each component.

For the neutron standard pulse, an exponential decay function with two exponential decay components was used, as shown in Eq. (3).

$$I_{\text{neutron}} = A_{n3}e^{-t/\tau_{n3}} + A_{n4}e^{-t/\tau_{n4}}, \quad (3)$$

where I_{neutron} is the amplitude of the neutron standard pulse from the maximum point to the end; τ_{n3} and τ_{n4} are the scintillation decay times for the V_k and STE mechanisms, respectively, and A_{n3} and A_{n4} are the amplitudes of each component.

Table 1 lists the fitting results for gamma- and neutron-induced CLYC emission. For the gamma waveform, the decay times are 2, 50, 420, and 3400 ns for the CVL, Ce^{3+}, V_k, and STE mechanisms, respectively. For the neutron waveforms, only V_k and STE are observed, with decays times of 390 and 1500 ns, respectively.

The decay times measured in our work, Refs. [10, 16], are listed in Table 2. The decay times in our work are essentially in agreement with the results from Ref. [10], except for the STE/neutron result, whereas the results from Ref. [16] were quite different from ours. Because the Ce^{3+} doping concentration was the same (0.5 mol%), these differences may be caused by different signal sample rates and signal recording lengths. Ref. [16] applied a sample rate of 250 Ms/s, which might be inadequate for obtaining accurate decay times. Thus, Ref. [16] showed longer decay times than our work (sample rate: 1 Gs/s) and Ref. [10] (sample rate: 2 Gs/s). The signal length recorded by the oscilloscope is 2 μs in this work, and in Ref. [10] it is 10 μs. The signal length of 2 μs is suitable for the gamma pulse, because its amplitude dropped almost to the baseline in 2 μs (Fig. 8, solid line). However, the neutron pulse, which has a longer decay time, requires a longer recording length than the gamma pulse to obtain the neutron decay times, especially for the STE mechanism.

Table 1 Fitting results for gamma- and neutron-induced CLYC emission

	CVL		Ce^{3+}		V_k		STE	
	τ (ns)	A	τ (ns)	A	τ (ns)	A	τ (ns)	A
Gamma	2	0.31	50	0.39	420	0.21	3400	0.07
Neutron	–	–	–	–	390	0.52	1500	0.49

4 Conclusion

The CLYC crystal has excellent properties and can play an important role in homeland security and nuclear safeguarding. Its capability of robust discrimination between neutrons and gamma rays makes CLYC a radiation detector with dual neutron and gamma-ray sensitivity [21, 22]. In this study, we evaluated the gamma-ray energy resolution and PSD capability of a CLYC crystal grown at BGRI. In addition, we obtained the decay times of different scintillation mechanisms by fitting decay functions to the neutron and gamma-ray waveform structures. The CLYC crystal has a gamma-ray energy resolution of $\sim$ 4.5% (FWHM) at 662 keV and has good PSD capability with a FoM of $\sim$ 2.6. Ultrafast scintillation decay ($\sim$ 2 ns) occurs in CLYC under gamma-ray excitation, whereas there is no evidence of ultrafast decay under thermal neutron excitation. To our knowledge, our CLYC crystal has superior PSD capability and an ultrafast decay time compared with other CLYC crystals in this area. It can be used in neutron–gamma dual-mode radiation detectors and can

Table 2 Measured decay times for gamma- and neutron-induced CLYC emission

References	Particle	CVL (ns)	Ce^{3+} (ns)	V_k (ns)	STE (ns)
This work	Gamma	2	50	420	3400
	Neutron	–	–	390	1500
[10]	Gamma	3	72	415	3470
	Neutron	–	–	393	3180
[16]	Gamma	48	280	730	5240
	Neutron	–	450	1420	6300

be applied to detect radiation in space. In the future work, we plan to grow CLYC crystals doped with enriched ^{6}Li (95%) with larger sizes and better properties by optimizing the crystal growth technology.

References

1. J. Glodo, R. Hawrami, K.S. Shah, Development of Cs_2LiYCl_6 scintillator. J. Cryst. Growth **379**, 73–78 (2013). https://doi.org/10.1016/j.jcrysgro.2013.03.023
2. C.M. Combes, P. Dorenbos, C.W.E. Van Eijk et al., Optical and scintillation properties of pure and Ce^{3+}-doped Cs_2LiYCl_6 and LiYCl6:Ce^{3+} crystals. J. Lumin. **82**, 299–305 (1999). https://doi.org/10.1016/S0022-2313(99)00047-2
3. E.V.D. Van Loef, P. Dorenbos, C.W.E. Van Eijk et al., Scintillation and spectroscopy of the pure and Ce^{3+}-doped elpasolites:Cs_2LiYX_6 (X = Cl; Br). J. Phys. Condens Matter. **14**, 8481–8496 (2002). https://doi.org/10.1088/0953-8984/14/36/307
4. A. Bessiere, P. Dorenbos, C.W.E. Van Eijk et al., New thermal neutron scintillators: Cs_2LiYCl_6: Ce and Cs_2LiYBr_6:Ce. IEEE Trans. Nucl. Sci. **51**, 2970–2972 (2004). https://doi.org/10.1109/TNS.2004.834957
5. A. Bessiere, P. Dorenbos, C.W.E. Van Eijk et al., Luminescence and scintillation properties of Cs_2LiYCl_6: Ce for γ and neutron detection. Nucl. Instrum. Methods A **537**, 242–246 (2005). https://doi.org/10.1016/j.nima.2004.08.018
6. E.V.D. Van Loef, J. Glodo, W.M. Higgins et al., Optical and scintillation properties of Cs_2LiYCl_6:Ce^{3+} and Cs_2LiYCl_6:Pr^{3+} crystals. IEEE Trans. Nucl. Sci. **52**, 1819–1822 (2005). https://doi.org/10.1109/TNS.2005.856812
7. P.A. Rodnyi, Core–valence luminescence in scintillators. Radiat. Meas. **38**, 343–352 (2004). https://doi.org/10.1016/j.radmeas.2003.11.003
8. K.N. Li, B.K. Li, M. Zhang et al., Real-time α/γ pulse shape discrimination in CsI(Tl) scintillators. Acta. Phys. Sin. **63**, 202901 (2014). https://doi.org/10.7498/aps.63.202901
9. N.D. Olympia, P. Chowdhury, C.J. Guess et al., Optimizing CLYC for fast neutron spectroscopy. Nucl. Instrum. Methods A **694**, 140–146 (2012). https://doi.org/10.1016/j.nima.2012.07.021
10. B.S. Budden, L.C. Stonehill, J.R. Terry et al., Characterization and investigation of the thermal dependence of CLYC waveforms. IEEE Trans. Nucl. Sci. **60**, 946–951 (2013). https://doi.org/10.1109/TNS.2012.2215884
11. R. Machrafi, N. Khan, A. Miller, Response functions of Cs_2LiYCl_6: Ce scintillator to neutron and gamma radiation. Radiat. Meas. **70**, 5–10 (2014). https://doi.org/10.1016/j.radmeas.2014.07.010
12. M.M. Bourne, C. Mussi, E.C. Miller et al., Characterization of the CLYC detector for neutron and photon detection. Nucl. Instrum. Methods A **736**, 124–127 (2014). https://doi.org/10.1016/j.nima.2013.10.030
13. K. Yang, P.R. Menge, Pulse shape discrimination of Cs_2LiYCl_6:Ce^{3+} scintillator from – 30 °C to 180 °C. Nucl. Instrum. Methods A **784**, 74–79 (2015). https://doi.org/10.1016/j.nima.2014.08.031
14. A. Giaz, N. Blasi, C. Boiano et al., Fast neutron measurements with ^{7}Li and ^{6}Li enriched CLYC scintillators. Nucl. Instrum. Methods A **825**, 51–61 (2016). https://doi.org/10.1016/j.nima.2016.03.090
15. D.W. Lee, L.C. Stonehill, A. Klimenko et al., Pulse-shape analysis of CLYC scintillator for neutron and gamma-ray discrimination. Nucl. Instrum. Methods A **664**, 1–5 (2012). https://doi.org/10.1016/j.nima.2011.10.013
16. N.D. Olympia, P. Chowdhury, C.J. Lister et al., Pluse shape analysis of CLYC for thermal neutrons, fast neutron, and gamma-rays. Nucl. Instrum. Methods A **714**, 121–127 (2013). https://doi.org/10.1016/j.nima.2013.02.043
17. J. Glodo, W.M. Higgins, E.V.D. Van Loef et al., Scintillation properties of 1 inch Cs_2LiYCl_6:Ce^{3+} crystals. IEEE Trans. Nucl. Sci. **55**, 1206–1209 (2008). https://doi.org/10.1109/TNS.2007.913467
18. J. Glodo, W.M. Higgins, E.V.D. Van Loef et al., Cs_2LiYCl_6:Ce^{3+} scintillator for nuclear monitoring applications. IEEE Trans. Nucl. Sci. **56**, 1257–1261 (2009). https://doi.org/10.1109/TNS.2009.2012515
19. W.M. Higgins, J. Glodo, U. Shirwadkar et al., Bridgman growth of Cs_2LiYCl_6:Ce^{3+} and ^{6}Li-enriched Cs_2LiYCl_6:Ce^{3+} crystals for high resolution gamma ray and neutron spectrometers. J. Cryst. Growth **312**, 1216–1220 (2010). https://doi.org/10.1016/j.jcrysgro.2009.09.046
20. M.B. Smith, T. Achtzehn, H.R. Andrews et al., Fast neutron spectroscopy using Cs_2LiYCl_6:Ce(CLYC) scintillator. IEEE Trans. Nucl. Sci. **60**, 855–859 (2013). https://doi.org/10.1109/TNS.2012.2219068
21. A. Giaz, L. Pellegri, F. Camera et al., The CLYC-6 and CLYC-7 response to γ-rays, fast and thermal neutrons. Nucl. Instrum. Methods A **810**, 132–139 (2016). https://doi.org/10.1016/j.nima.2015.11.119
22. C.M. Whitney, L. Soundara-Pandian, E.B. Johnson et al., Gamma–neutron imaging system utilizing pulse shape discrimination with CLYC. Nucl. Instrum. Methods A **784**, 346–351 (2015). https://doi.org/10.1016/j.nima.2014.09.022